Atomic scale mobility of the volatile fission products Xe, Kr and I in cubic SiC

M. W. D. Cooper, S. Kelly, M. Bertolus

Atomic scale mobility of the volatile fission products Xe, Kr and I in cubic SiC

M.W.D. Cooper[a,b], S. Kelly[a,b], M. Bertolus*[b]

[a] *Department of Materials, Imperial College London, London, SW7 2AZ, UK*
[b] *CEA, DEN, DEC, Centre de Cadarache, 13108 Saint-Paul-Lez-Durance, France*

Abstract

The migration barriers for the vacancy-assisted migration of fission products in 3C-SiC are reported and analysed in the context of the five frequency model, which enables one to calculate an effective diffusion coefficient from elementary mechanisms. Calculations were carried out using the nudged elastic band method (NEB) with interatomic forces determined from density functional theory (DFT). Justification for treating vacancy-assisted fission product migration as limited to the FCC carbon sublattice is based on the stability of carbon vacancies, unfavourable silicon vacancy formation and the accommodation of fission products on the carbon sublattice. Results show that over the majority of the band gap the activation energy for I exceeds that of Xe which exceeds that of Kr. Results also indicate that activation energies are higher near the top of the band gap, thus, implying that enhanced fission product retention can be achieved through n-type doping of 3C-SiC, which limits the availability of the migration mediating carbon vacancies.

Keywords: Silicon Carbide, Fission Products, Diffusion, Density Functional Theory

1. Introduction

Silicon carbide (SiC) exhibits a very high melting point and good chemical stability making it suitable for high temperature applications. In particular, as a wide band gap semiconductor, it has been touted for applications in high temperature electronic devices [1] and is envisaged as an alternative to Si. Furthermore, it has a low neutron capture cross section making it an interesting candidate material in fission and fusion reactors. Low fission product mobility in SiC makes it a prime candidate material for a barrier in advanced high temperature reactor designs. For example, the tristructural-isotropic (TRISO) particle fuel design employs SiC in this role [4].

A significant body of work has been undertaken to study the release of radiologically important fission products from nuclear fuel. For example, rare gas fission products, Xe and Kr, are highly insoluble in the UO_2 matrix and are released from the fuel in significant quantities [5–10]. Similarly, highly volatile fission products, such as I and Cs, rapidly migrate out of the host UO_2 matrix [11, 12]. Therefore, these fission products can provide a particular problem for retention and must be isolated through a barrier layer. The mobility of fission products in SiC has been studied experimentally [4, 13–16] and atomic scale simulations can be employed to develop a fundamental understanding of the underlying mechanisms. Density functional theory (DFT) has been successfully applied to the investigation of defect behaviour in a number of nuclear materials [17]. SiC exhibits a large number of polytypes, the most common being the cubic

Email address: marjorie.bertolus@cea.fr (M. Bertolus*)

3C and the two hexagonal 4H and 6H structures. The 3C structure is simpler to model, while most experimental results have been obtained on 6H-SiC. Wiktor *et al.* [18] have shown that the extrapolation of the formation energies of point defects obtained in 3C-SiC to the gap of the 6H structure is a good approximation, especially for carbon defects.

In DFT [18, 19] and the GW [21] approximation carbon vacancies are predicted to be the most stable intrinsic defects in SiC. Unlike GW, DFT significantly underestimates the band gap. Nonetheless the same trends are predicted for the charge states and formation energies of intrinsic defects across the theoretical band gaps for both approaches. Therefore, DFT energies as a function of the Fermi level must be considered relative to the size of the bandgap.

The results of Wiktor *et al.* [18] indicated that the carbon vacancy is in the 2+ charge state over nearly the full theoretical band gap (1.38 eV), although at the top of the band gap the neutral carbon vacancy was predicted to be favourable. Previously Bertolus *et al.* [19] and Charaf-Eddin and Pizzagalli [20] used DFT to investigate the incorporation of a number of fission products into neutral defects of SiC, including Xe, Kr and I. The substitution of fission products onto the carbon sublattice was widely predicted to be very significantly more favourable than as an interstitial or on the Si sublattice. Similarly, Roma *et al.* [22] identified that Pd is preferentially accommodated on carbon sublattice either as a +2 or a neutral defect. Furthermore, the migration of Pd in SiC was also predicted to be restricted to vacancy-assisted migration on the FCC carbon sublattice when vacancies are present [23].

Here we investigate the mobility of Xe, Kr and I in 3C-SiC from their stable sites on the carbon sublattice by assuming a vacancy-assisted migration mechanism like that of Roma *et al.* [22]. This is justified because i) the most stable sites for these fission products are on the carbon sublattice, ii) the carbon vacancy is the most stable defect in SiC and iii) the highly unfavourable silicon vacancy is predicted to be converted to a carbon vacancy C_{Si} antisite pair (see Figure 1).

This allows an analysis of fission product mobility that is based on the five frequency model for vacancy-assisted diffusion on the FCC carbon sublattice. The regimes over which diffusion via +2 or neutral carbon vacancies is suitable are also discussed.

2. Methodology

2.1. Calculation parameters

All DFT calculations were carried out using the projector augmented wave (PAW) method [26, 27] as implemented in the Vienna *ab initio* Simulation Package (VASP) [28–30] with a plane wave cut-off energy of 600 eV. For carbon the $2s$ and $2p$ levels are treated as valence states (and level $1s$ is included in the core regions), whereas for silicon $3s$ and $3p$ are considered to be valence states (and the $1s$, $2s$ and $3p$ levels constitute the core region). The parametrisation of Perdew, Burke and Ernzerhof (PBE) [31] for the Generalised Gradient Approximation (GGA) was used to describe the exchange-correlation interactions. Defect calculations were carried out on supercells of 3×3×3 sphalerite unit cells of SiC (216 atoms) with spin polarisation and no conservation of symmetry. The Brillouin zone was sample using a 2×2×2 k-point mesh generated using the Monkhorst-Pack scheme [32]. Electron relaxation was optimised in reciprocal space with force and total energy convergence criteria of 10^{-8} eVÅ^{-1} and 10^{-8} meV respectively. The perfect crystal properties predicted here are compared to experimental results in Table 1, showing a good agreement. Similar calculation parameters were used previously by Wiktor *et al.* [18] to determine the positron lifetimes and the results showed a strong agreement with experiment. In addition, the insertion of Kr and Xe in SiC is correctly described using the PBE functional [19].

The formation energy of a charged defect was calculated by:

$$E_F = E_{tot}(V_{X,q}) - n_C\mu_{\mathrm{SiC}}^{bulk} - (n_{\mathrm{Si}} - n_{\mathrm{C}})\left[\mu_{\mathrm{Si}}^{bulk} + \frac{1}{2}\Delta H_f(\mathrm{SiC})\right] + q(E_{VBM} + \mu_e) \quad (1)$$

where E_{tot} is the energy of the defective supercell, μ_{SiC}^{bulk} is the energy per SiC pair in the bulk, the energy per atom in bulk Si is μ_{Si}^{bulk}. The Fermi level is given by μ_e and E_{VBM} is the energy of the valence band maximum. The formation enthalpy of SiC, $\Delta H_f(\mathrm{SiC})$, is given by:

$$\Delta H_f(\mathrm{SiC}) = \mu_{\mathrm{SiC}}^{bulk} - \mu_{\mathrm{Si}}^{bulk} - \mu_{\mathrm{C}}^{bulk} \quad (2)$$

where μ_C^{bulk} is defined as the energy of a carbon atom within the diamond structure.

One issue with using the supercell approach for charged defects is the unphysical system charge that arises due periodic boundary conditions. A charge neutralising background jellium must, therefore, be used [33–35]. However, defect energies must be adjusted according to the interaction energy of a periodically repeating system containing a point charge, q, with the neutralising background jellium, as defined by the Madelung energy [33, 34]:

$$\Delta E_{el}(q) = \frac{\alpha q^2}{2\epsilon L} \quad (3)$$

where α is the Madelung constant ($\alpha = 1.6381$ for 3C-SiC), ϵ is permittivity of the medium and L is the supercell size length. ϵ and L are defined from the geometry optimised perfect cell (Table 1). To calculated the additional potential correction term ΔV the method of Taylor and Bruneval [36] is used, such that:

$$\Delta V = \langle v_{KS}^{bulk}\rangle - \langle v_{KS}^{defect}\rangle \quad (4)$$

where $\langle v_{KS}^{bulk}\rangle$ and $\langle v_{KS}^{defect}\rangle$ are the averaged Kohn-Sham potentials for the perfect and defective supercells respectively.

Migration barriers are calculated using the nudged elastic band (NEB) method [37] in conjunction with the same DFT parameters described above. For each NEB calculation the initial and final stable configurations of a given transition are determined using geometry optimisation. Based on the linear interpolation of the initial and final atomistic configurations an initial guess of the lowest migration pathway, which is then minimised, is made at five discrete points. There are, as such, seven images of the lowest energy migration pathway including the initial and final configurations.

2.2. Five Frequency Model

Based on the justifications given in section 1 it assumed that fission product migration is restricted to the FCC carbon sublattice. The five frequency model governing vacancy mediated impurity diffusion on an FCC lattice assumes that the second nearest neighbour distance is great enough so the vacancy-impurity binding is very low and can be neglected beyond this distance [38]. Therefore diffusion can be broken down into five constituent individual jump frequencies [39, 40]:

- w_0 - vacancy-atom exchange rate in the host material. Vacancy migration in the bulk whereby the bulk is defined as any jump not involving the first nearest neighbour site with respect to the impurity. In Figure 2 w_0 is represented by the blue arrow between the second and third nearest neighbour positions on the carbon sublattice.

- w_1 - rotation rate of the impurity-vacancy pair. The jump of a vacancy around the impurity between two first nearest neighbour sites, as represented by the yellow arrow in Figure 2.
- w_2 - impurity-vacancy exchange rate. The jump of the impurity into a vacancy that is occupying a first nearest neighbour site, as indicated by the red arrow in Figure 2.
- w_3 - dissociation rate of the impurity-vacancy pair. The jump of the vacancy from a first nearest neighbour position to a second nearest neighbour site. The purple arrow in Figure 2 represents dissociation.
- w_4 - association rate of the impurity-vacancy pair. Vacancy migration from a second nearest neighbour position into a first nearest neighbour site with respect to the impurity as indicated by the green arrow in Figure 2.

Each of the above jump frequencies, w_i, has an associated attempt frequency, v_i, and energy barrier, E_i, such that:

$$w_i = v_i.\exp\left(\frac{-E_i}{k_B T}\right) \tag{5}$$

where k_B is the boltzmann constant and T is the temperature. Generally, impurity diffusivity, D, can be described by:

$$D = \frac{1}{6} f \alpha^2 p v_2.\exp\left(\frac{-E_2}{k_B T}\right) \tag{6}$$

where α is the jump distance for the vacancy-impurity exchange and p is the probability of finding a vacancy in a first nearest neighbour site with respect to the impurity, which can be expressed as follows:

$$p = N.\exp\left(\frac{-(E_f + E_B)}{k_B T}\right) \tag{7}$$

where E_f is the bulk vacancy formation energy, E_B is the impurity-vacancy binding energy and N is the number of first nearest neighbour sites with respect to the impurity. In the absence of interaction beyond the first nearest neighbour, the binding energy can be calculated by $E_B = E_4 - E_3$. As such, if the vacancy and impurity attract ($E_B < 0$) the probability of finding a vacancy in a first nearest neighbour site is enhanced with respect to the bulk concentration. Equation 8 shows that the correlation factor, f, as a function of w_1, w_2, w_3 and the escape probability, $\frac{7F_3}{2}$ [39]:

$$f = \frac{w_1 + 7F_3 w_3/2}{w_1 + w_2 + 7F_3 w_3/2} \tag{8}$$

Although an explicit form of the escape probability, $\frac{7F_3}{2}$, is given in reference [39], the results of NEB calculations presented later show that for all cases studied here the association rate, w_4, far exceeds that of bulk vacancy migration, w_0. Consequently, every time the vacancy dissociates from the impurity it rapids re-associates and the escape probability, $\frac{7F_3}{2}$, tends to zero so that:

$$f = \frac{w_1}{w_1 + w_2} \tag{9}$$

Therefore, in conjunction with strong vacancy-impurity binding, the migrating species can be treated as a bound pair with some special cases discussed below:

a) if $w_1 >> w_2$ vacancy migration around the impurity is significantly greater than impurity-vacancy exchange. This effectively randomises the position of the vacancy with respect to the impurity before the impurity jumps into the vacant site. As such, $f \rightarrow 1$ in equation 6, so that the impurity diffusivity is expressed as:

$$D = \frac{1}{6}\alpha^2 v_2 N \exp\left(\frac{-(E_2 + F_f + E_B)}{k_B T}\right) \tag{10}$$

b) if $w_2 >> w_1$ the impurity-vacancy exchange rate is far greater than the other jump frequencies. Consequently, the motion of the impurity is highly correlated as it 'rattles' back and fourth between two adjacent lattice sites. Therefore, equation 9 gives $f \rightarrow \frac{w_1}{w_2}$ and by assuming all attempt frequencies (v_i) are approximately equal to the Debye frequency the impurity diffusivity is expressed as:

$$D = \frac{1}{6}\alpha^2 v_1 N \exp\left(\frac{-(E_1 + E_f + E_B)}{k_B T}\right) \tag{11}$$

Long range diffusion is, therefore, dependent on the ability of the vacancy-impurity pair to reconfigure by rotation (w_1).

c) if $w_2 \approx w_1$ there is a combined correlated impurity-vacancy exchange/rotation mechanism, whereby $f \rightarrow \frac{1}{2}$ and the diffusivity is expressed as:

$$D = \frac{1}{12}\alpha^2 v_{1,2} N \exp\left(\frac{-(E_{1,2} + E_f + E_B)}{k_B T}\right) \tag{12}$$

This work is concerned firstly with identifying the stable configurations associated with the five frequency model and then determining all migration barriers between these configurations (E_0, E_1, E_2, E_3, E_4 and E_5). Based on the special cases outline above an analysis of the vacancy-assisted migration mechanisms for Xe, Kr and I migration in cubic SiC is given.

3. Results and discussion

3.1. Formation energies and charge states

Formation energies are reported as a function of μ_e in Figure 3 for a carbon vacancy and a first nearest neighbour carbon divacancy. Values are reported from the bottom of the band gap up to edge of the experimental band gap (2.39 eV), however, as the computational band gap is just 1.38 eV one must consider the defect energies at the top of the theoretical band gap as commensurate with top of the real life band gap (see section 1), as shown by comparison with GW results [21], which show the same trends from $0 < \mu_e < 2.39$ as predicted by DFT from $0 < \mu_e < 1.38$. Figure 3 indicates that over the calculated band gap the +2 charged supercell dominates for both the single carbon vacancy and the carbon divacancy. However, at the top of the theoretical band gap the neutral supercell becomes favourable. It is only when the Fermi level significantly exceeds that of the computational band gap that any negative charge states exist for carbon vacancy type defects.

As for the carbon vacancies, a Xe impurity occupying a carbon site, Xe_C, is also dominated by the +2 charged supercell over the full calculated band gap (see Figure 4a). Alternatively, if the xenon impurity has an additional carbon vacancy in a first nearest neighbour carbon site the neutral charge state becomes favourable at the top of the band gap (see Figure 4b). Again one only encounters alternative charge states when μ_e is significantly greater than 1.38 eV.

Due to similar chemistry the Kr formation energies are very similar to that of Xe; the +2 charged defects dominate over the the full computational band gap (see Figure 5). However, if a carbon vacancy occupies a first nearest neighbour carbon site to the Kr impurity the neutral supercell becomes favourable near the top of the computational band gap.

Figure 6 shows that the accommodation of I at a carbon site is also dominated by the the +2 charge state over nearly the full theoretical band gap. If the first nearest neighbour carbon site with respect to the impurity is vacant the +2 supercell is also more favourable over a broad range of Fermi levels. However, near the top of the theoretical band gap alternative valence states become favourable.

For all defects studied here that are involved in the five-frequency model on the carbon sublattice it is clear that the +2 charge state is dominant over a broad range of the computation band gap. However, the neutral charge state is important near the top of the bad gap for the formation of the migration mediating carbon vacancies as well as for the accommodation of the noble gases Xe and Kr. Therefore, all migration barriers involved in the five-frequency model will be examined in both the neutral and the +2 charged supercells.

3.2. Migration barriers of the five-frequency model

The stable configurations calculated in section 3.1 define the initial and final configurations for E_0, E_1 and E_2. Whilst the initial configurations for E_3 and E_4 is given by the impurity-vacancy first nearest neighbour configuration determined previously, the final configuration was calculated by energy minimisation of the impurity-vacancy second nearest neighbour configuration. Using these initial and final configurations the NEB method was used to calculate the energy barriers.

For summary the energy barriers associated with the five frequency model (i.e. E_{0-4}) for I, Xe and Kr are shown in Table 2. The charge neutral and +2 supercell cases are both reported. Firstly, one should note that in all cases $E_4 < E_0$ (or $w_4 >> w_0$) so that if the vacancy overcomes the binding energy with the impurity to reach a second nearest neighbour site it is highly likely that it will re-associate with the impurity rather than migrate into the bulk. Additionally, all cases exhibit strong binding energies ($E_3 > E_4$) in line with the limiting cases discussed at the end of section 2.2. Therefore, the relative height of the E_1 and E_2 energy barriers determine the specific limiting case.

Figure 7 shows the E_1 and E_2 barriers associated with the five frequency model for Xe in the neutral supercell regime, indicating $E_1 > E_2$. Consequently, the extremely high dependency of the jump frequency on the energy barrier (equation 5) dictates that $w_2 >> w_1$. The diffusivity is therefore determined by equation 11, such that E_1 is the only barrier that contributes to the activation energy. Although for the case of xenon in the +2 charged supercell the migration barriers are different, the same relative trends between barriers are predicted - i.e. $w_2 >> w_1$. Therefore, the migration mechanism remains the same as for the neutral case and E_1 plays the dominant role in governing migration.

The energy barriers for carbon vacancy mediated Kr migration in 3C-SiC are shown in Figure 8. As with Xe, the migration mechanism for Kr in the neutral supercell is predicted to proceed through the rotation of a tightly bound vacancy-impurity pair where E_1 contributes to the activation energy. However, in the +2 charged supercell $E_1 \approx E_2$ (at least within 0.04 eV) so that $w_1 \approx w_2$. In this case, the similar jump frequencies of impurity-vacancy exchange and rotation leads to a somewhat correlated motion, such that $f \rightarrow \frac{1}{2}$ and $E_2 \approx E_1$ contributes to the activation energy (equation 12).

Figure 9 shows the energy barriers associated with the five frequency model for I in the neutral supercell regime, indicating that $E_1 > E_2$ or $w_2 >> w_1$. In addition to the high binding energy, this reveals a migration mechanism that is again characterised by a tightly bound impurity-vacancy pair that rotates through the lattice. The diffusivity is, thus, determined by equation 11.

Although the barriers are different, the same trends and mechanism are predicted for the +2 supercell.

In summary, nearly all of the cases studied exhibit a type b) migration mechanism (see section 2.2), whereby, the impurity rattles between the two carbon sites and the rotation of this tightly bound impurity-vacancy pair provides the means of diffusion. Kr in the +2 supercell exhibits some mixture of a) and b) type migration with a somewhat correlated diffusive motion. Based on these limiting cases the activation energies can be determined.

3.3. Activation energies

Table 3 summarises the activation energies for I, Xe and Kr for the neutral and +2 supercells calculated using equation 11 except for the case of Kr in the +2 charged supercell, where equation 12 is used. In the cases of the charged supercell the formation energy of the mediating carbon vacancy is dependent on the Fermi level, μ_e, and, therefore, so is the activation energy. We have, thus, reported the activation energy as function of the Fermi level (see Table 3).

In line with previous simulations [18], it was predicted in section 3.1 that the transition between +2 and neutral carbon vacancies occurs at $\mu_e = 1.33$ eV (see Figure 3). This indicated that the +2 regime is expected to dominate over the majority of the bandgap. Thus, one may promote high activation energies by favouring n-type doping, so long as one does not raise the Fermi level to the top region of the band gap where neutral vacancies begin to dominate. In the p-doping regimes (i.e. near the bottom of the band gap) the activation energy is lowest in part to the low formation energy of the migration mediating carbon vacancies.

Xe has a higher activation energy than Kr across the entire band gap. Due to their similar inert chemistry this difference can be attributed to size effects. In the +2 regime it can be seen that, although the impurity-vacancy exchange barrier (E_2) is lower for Xe, the diffusion limiting impurity-vacancy rotation barrier (E_1) is in fact 0.46 eV lower for Kr. This is sufficient to ensure Kr has a lower activation energy in the +2 supercell despite the tighter binding ($E_4 - E_3$) for Xe. In the neutral supercell Kr has a more attractive binding energy in addition to a lower rate limiting diffusion barrier, thus, contributing an even lower Kr activation energy compared to that of Xe. These results indicate that Kr will diffusion more rapidly than Xe regardless of the Fermi level.

Over the majority of the band gap (+2 regime) I exhibits the highest activation energy, indicating that it will diffuse more slowly than the noble gases. Early results from experimental studies reflect this, in that I has been observed to be immobile in SiC up to 1400 °C [41], whereas, Xe exhibits limited mobility at 1350-1400 °C [42]. However, Figure 10 indicates that at the very top the band gap it is possible that iodine mobility could exceed that of Xe. This is a consequence of the reduced E_1 barrier for I in the neutral cell compared to the +2 supercell, whereas, the converse is true for the noble gases (see Table 2). This highlights a key way in which the chemistry of a given species affects mobility as function of the Fermi level and indicates how doping can manipulate the efficacy of SiC for fission product retention.

4. Conclusions

Density functional theory has been applied to investigate the vacancy-assisted migration of fission products in 3C-SiC. Based on the stable carbon vacancies and the accommodation of fission products on the carbon sublattice, a justification is made for treating diffusion as limited to the FCC carbon sublattice. Furthermore, the +2 and neutral charge states are sufficient to describe the defects involved over the full theoretical band gap. All migration barriers involved in the five frequency model have been calculated for Xe, Kr and I in the +2 and neutral supercells.

Results indicate that over the majority of the band gap the activation energy for I exceeds that of Xe which exceeds that of Kr. It is expected therefore that SiC is most effective at preventing I mobility, as supported by preliminary experimental results [41, 42].

The activation energy for all species increases as a function of the Fermi level, indicating that n-type doping could be used to enhance the fission product retention properties of SiC. Raising the Fermi level reduces the stability carbon vacancies, thus, limiting their availability for assisting migration. Further work should be done to investigate the attempt frequencies involved in the five frequency model for a full description of fission product diffusivity. Additionally, models that incorporate more mechanisms involving longer range interactions must also be studied.

Acknowledgements

R.W. Grimes and E. Vathonne are acknowledged for useful discussion. Part of this work was performed using HPC resources from GENCI (grant t2013086922).

References

[1] Willander, M., Friesel, M., Wahab, Q. U. and Straumal, B. (2006) *J. Mater. Sci. Mater. Electron.* **17**, 1–25.

[2] Giancarli, L., Ferrari, M., Fütterer, M. A. and Malang, S. (2000) *Fusion Eng. Des.* **49-50**, 445–456.

[3] Yvon, P. and Carré, F. (2009) *J. Nucl. Mater.* **385**, 217–222.

[4] Mehner, A. W., Heit, W., Röllig, K., Ragoss, H. and Müller, H. (1990) *J. Nucl. Mater.* **171**, 9–18.

[5] Shirsat, A. N., Ali (Basu), M., Kolay, S., Datta, A. and Das, D. (2009) *J. Nucl. Mater.* **392**, 16–21.

[6] Yun, Y., Oppeneer, P. M., Kim, H. and Park, K. (2009) *Acta Mater.* **57**, 1655–1659.

[7] Turnbull, J. A. and Friskney, C. A. (1982) *J. Nucl. Mater.* **107**, 168–184.

[8] Ball, R. G. J. and Grimes, R. W. (1990) *J. Chem. Soc. Faraday Trans.* **86**, 1257–1261.

[9] Matzke, H. J. (1980) *Radiat. Eff.* **53**, 219–242.

[10] Andersson, D. A., Garcia, P., Liu, X.-Y., Pastore, G., Tonks, M., Millett, P., Dorado, B., Gaston, D. R., Andrs, D., Williamson, R. L., Martineau, R. C., Uberuaga, B. P. and Stanek, C. R. (2014) *J. Nucl. Mater.* **451**, 225–242.

[11] Grimes, R. W., Balls, R. G. J. and Catlow, C. R. A. (1992) *J. Phys. Chem. A* **53**, 475–484.

[12] Ball, R. G. J., Burns, W. G., Henshaw, J., Mignanelli, M. A. and Potter, P. E. (1989) *J. Nucl. Mater.* **167**, 191–204.

[13] Minato, K., Ogawa, T., Kashimura, S. and Fukuda, K. (1990) *J. Nucl. Mater.* **172**, 184–196.

[14] Vincent, L., Sauvage, T., Carlot, G., Garcia, P., Martin, G., Barthe, M. F. and Desgardin, P. (2009) *Vacuum* **83**, 36–39.

[15] Minato, K., Ogawa, T., Fukuda, K., Shimizu, M., Tayama, Y. and Takahaski, I. (1994) *J. Nucl. Mater.* **208**, 266–281.

[16] Petti, D. A., Buongiorno, J., Maki, J. T., Miller, G. K. and Hobbins, R. R. (2003) *Nucl. Eng. Des.* **222(2-3 SPEC)**, 281–297.

[17] Bertolus, M., Freyss, M., Dorado, B., Martin, G., Hoang, K., Maillard, S., Skorek, R., Garcia, P., Valot, C., Chartier, A., Van Brutzel, L., Fossati, P., Grimes, R. W., Parfitt, D. C., Bishop, C. L., Murphy, S. T., Rushton, M. J. D., Staicu, D., Yakub, E., Nichenko, S., Krack, M., Devynck, F., Ngayam-Happy, R., Govers, K., Deo, C. S. and Behera, R. K. (2015) *J. Nucl. Mater.* **462**, 475–495.

[18] Wiktor, J., Jomard, G., Torrent, M. and Bertolus, M. (2013) *Phys. Rev. B* **87**, 235207.

[19] Bertolus, M. *Modélisation à l'échelle atomique de matériaux nucléaires du cycle du combustible*, Technical report CEA-R-6281 (2011).

[20] Charaf-Eddin, A. and Pizzagalli, L. (2012) *J. Nucl. Mater.* **429**, 329–332.

[21] Bruneval, F. (2012) *Nucl. Instruments Methods Phys. Res. Sect. B Beam Interact. with Mater. Atoms* **277**, 77–79.

[22] Roma, G. (2009) *J. Appl. Phys.* **106**, 123504.

[23] Shrader, D., Khalil, S. M., Gerczak, T., Allen, T. R., Heim, A. J., Szlufarska, I. and Morgan, D. (2011) *J. Nucl. Mater.* **408**, 257-271.

[24] Wang C., Bernholc J. and Davis, R. F. (1988) *Phys. Rev. B* **38**, 12752.

[25] Gao, F., Bylaska, E. J., Weber, W. J. and Corrales, L. R. (2001) *Phys. Rev. B* **64**, 245208.

[26] Blöchl, P. E. (1994) *Phys. Rev. B* **50**, 17953–17979.

[27] Kresse, G. (1999) *Phys. Rev. B* **59**, 1758–1775.

[28] Kresse, G. and Hafner, J. (1993) *Phys. Rev. B* **47**, 558–561.

[29] Kresse, G. and Hafner, J. (1994) *Phys. Rev. B* **49**, 14251–14269.

[30] Kresse, G. and Furthmüller, J. (1996) *Comput. Mater. Sci.* **6**, 15–50.

[31] Perdew, J. P., Burke, K. and Ernzerhof, M., (1996) *Phys. Rev. Lett.* **77**, 3865–3868.

[32] Monkhorst, H. J. and Pack, J. D. (1976) *Phys. Rev. B* **13**, 1748–1749.

[33] Leslie, M. (1985) *J. Phys. C: Solid State Phys.* **18**, 973-982.

[34] Makov, G. and Payne, M. C. (1995) *Phys. Rev. B* **51**, 4014-4022.

[35] Murphy, S. T. and Hine, N. D. M. (2013) *Phys. Rev. B* **87**, 094111.

[36] Taylor, S. E. and Bruneval, F. (2011) *Phys. Rev. B* **84**, 075155.

[37] Henkelman, G., Uberuaga, B. P. and Hine, J. (2000) *J. Chem. Phys.* **113**, 9901.

[38] Lucas, G. and Pizzagalli, L. (2007) *J. Phys.: Condens. Matter* **19**, 086208.

[39] Manning, J. (1964) *Phys. Rev.* **136**, 1758–1766.

[40] Mehrer, H (2007) Diffusion in Solids, Springer-Verlag Berlin Heidelberg.

[41] Carlot, G, private communication.

[42] Gilabert, E (2012) GdR MATINEX plenary meeting.

[43] Lee, D. H. and Joannopoulos, J. D. (1982) *Phys. Rev. Lett.* **48**, 1846.

[44] Choyke, W. J., Hamilton, D. R. and Patrick, L. (1964) *Phys. Rev.* **133**, 1163–1166.

[45] Patrick, L. and Choyke, W. J. (1970) *Phys. Rev. B* **2**, 2255–2256.

Figures and Tables

Table 1: The bulk properties of 3C-SiC predicted using the DFT method in this work and from previous experimental work [43–45].

	DFT (present work)	Experimental
Lattice parameter	4.379 Å	4.36 Å [43]
Band gap	1.38 eV	2.39 eV [44]
Relative dielectric constant, ϵ_r	9.72 Fm^{-1}	9.72 Fm^{-1} [45]

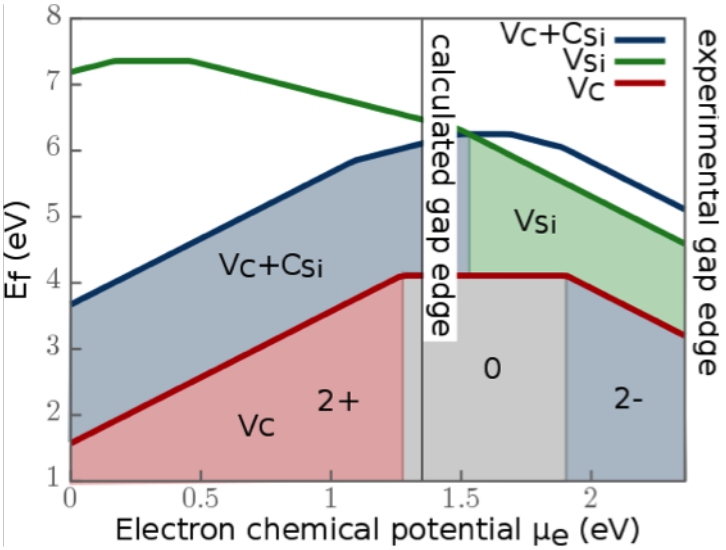

Figure 1: The formation energy for the carbon vacancy, a carbon vacancy C_{Si} antisite pair and a silicon vacancy as a function of the Fermi level. Values are reported up to the experimental band gap limit of 2.39 eV. The calculated band gap limit of 1.38 eV is shown by the dotted line. Data for Figure taken in reference [18].

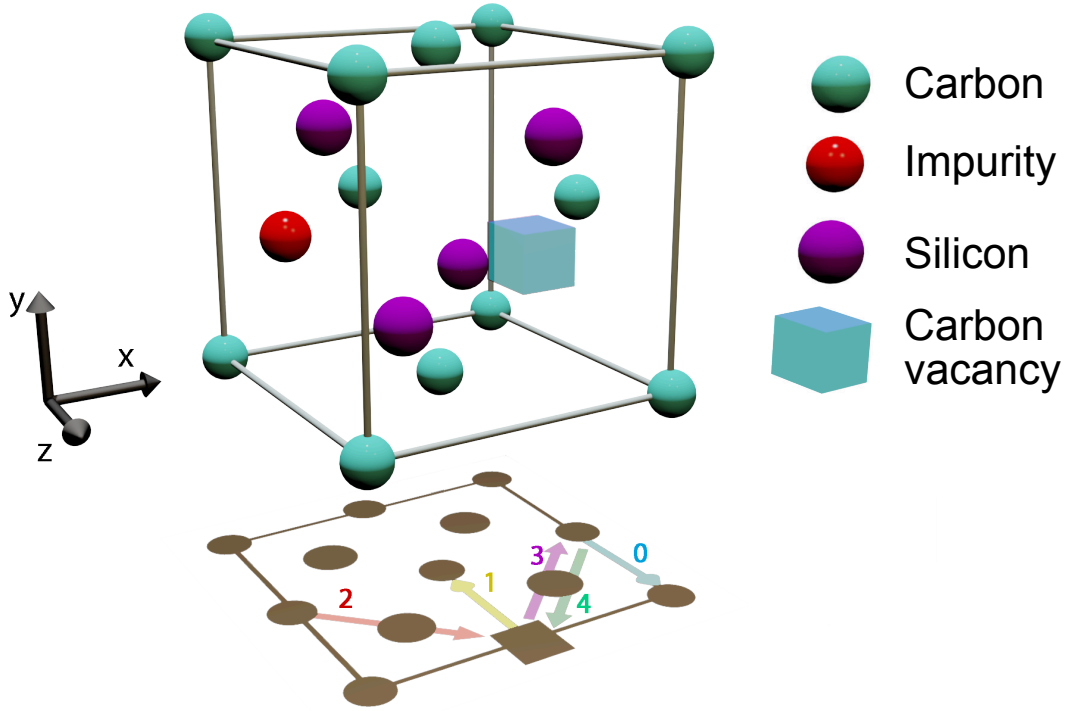

Figure 2: The jumps involved in the the five frequency model are indicated using coloured arrows: i) w_0 (blue) - vacancy migration in the bulk (beyond the first nearest neighbour), ii) w_1 (yellow) - vacancy migration between two first nearest sites with respect to the impurity, iii) w_2 (red) - the migration of the impurity into the vacancy, iv) w_3 (purple) - vacancy migration from the first nearest neighbour site to the second nearest neighbour site, v) w_4 (green) - vacancy migration from the second nearest neighbour site to the first nearest neighbour site. Silicon and carbon are represented by purple and turquoise spheres respectively. The red sphere indicates the impurity atom (Xe, Kr or I).

Table 2: The energy barriers for Xe, Kr and I associated with the jump frequencies of the five-frequency model, as shown in Figure 2. Values are reported for the charge neutral and +2 supercells. Note that $E_B = E_4 - E_3$.

		Neutral				Charged +2			
Label	Reaction	V_C	Xe	Kr	I	V_C	Xe	Kr	I
E_0	Host vacancy-atom exchange	3.42	-	-	-	5.54	-	-	-
E_1	Impurity-vacancy rotation	-	4.01	3.30	3.55	-	3.64	3.18	3.96
E_2	Impurity-vacancy exchange	-	3.87	3.34	3.00	-	2.68	2.69	3.63
E_3	Impurity-vacancy dissociation	-	5.32	3.81	4.24	-	4.58	4.63	4.63
E_4	Impurity-vacancy association	-	2.65	0.97	1.23	-	3.02	3.17	3.75

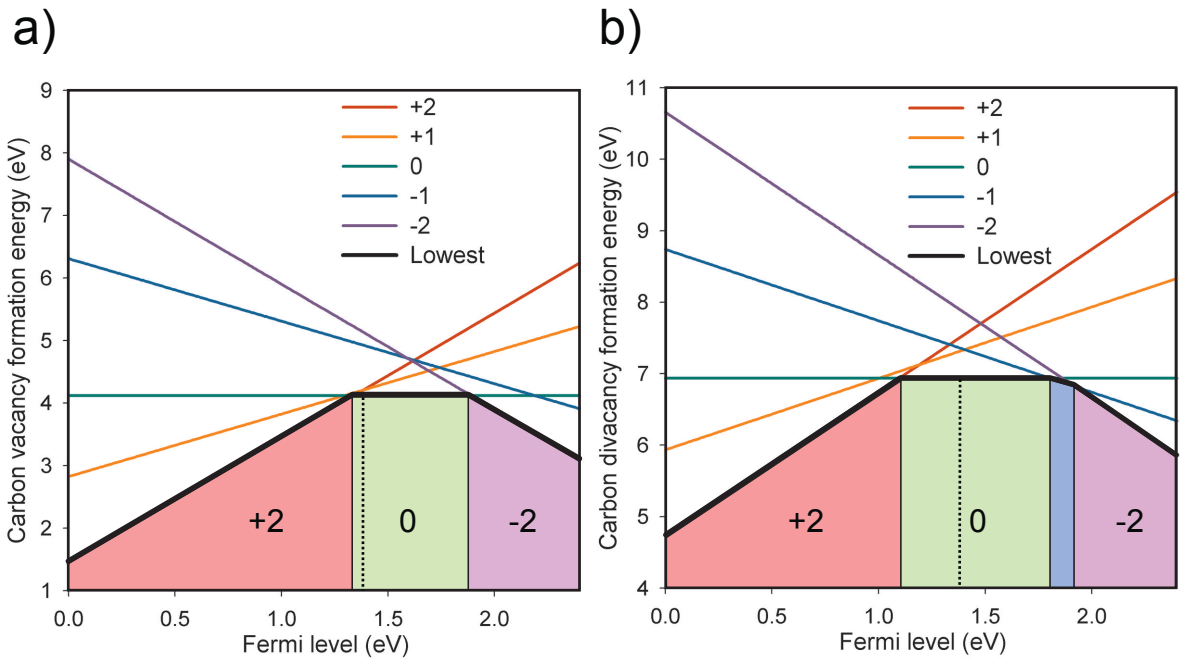

Figure 3: The formation energy for a) the carbon vacancy and b) carbon divacancy as a function of the Fermi level. Values are reported up to the experimental band gap limit of 2.39 eV. The calculated band gap limit of 1.38 eV is shown by the dotted line.

Table 3: The activation energy for I Kr and Xe in the charge neutral and 2+ supercells. These activation energies are also reported in Figure 10.

Impurity	Neutral	Charged +2
Xe	$E_f + E_B + E_1 = 5.45$	$E_f + E_B + E_1 = 3.29 + 2\mu_e$
Kr	$E_f + E_B + E_{1,2} = 4.60$	$E_f + E_B + E_1 = 2.92 + 2\mu_e$
I	$E_f + E_B + E_1 = 4.65$	$E_f + E_B + E_1 = 4.27 + 2\mu_e$

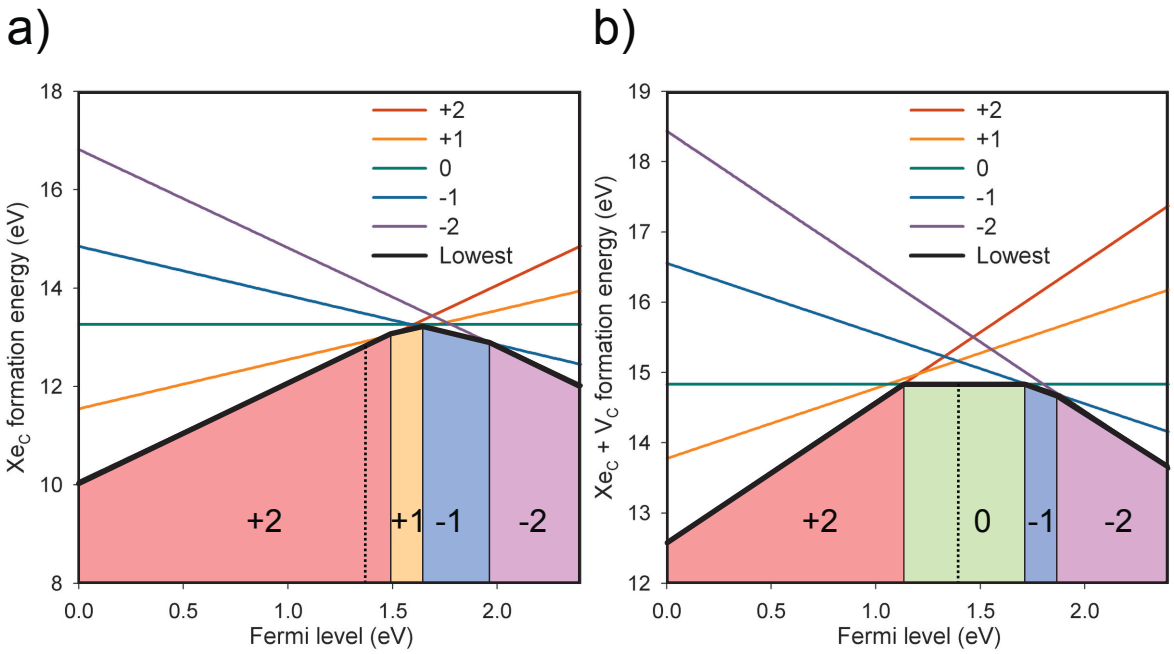

Figure 4: The formation energy for the accommodation of Xe at a) the carbon vacancy and b) carbon divacancy as a function of the Fermi level. Values are reported up to the experimental band gap limit of 2.39 eV. The calculated band gap limit of 1.38 eV is shown by the dotted line.

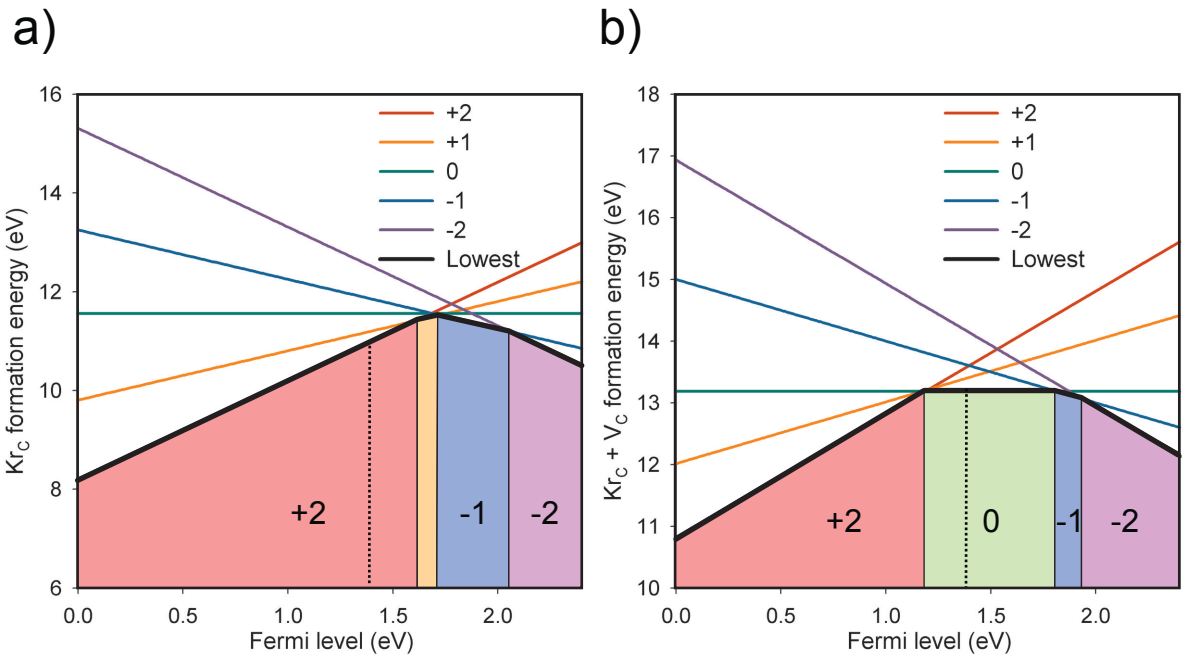

Figure 5: The formation energy for the accommodation of Kr at a) the carbon vacancy and b) carbon divacancy as a function of the Fermi level. Values are reported up to the experimental band gap limit of 2.39 eV. The calculated band gap limit of 1.38 eV is shown by the dotted line.

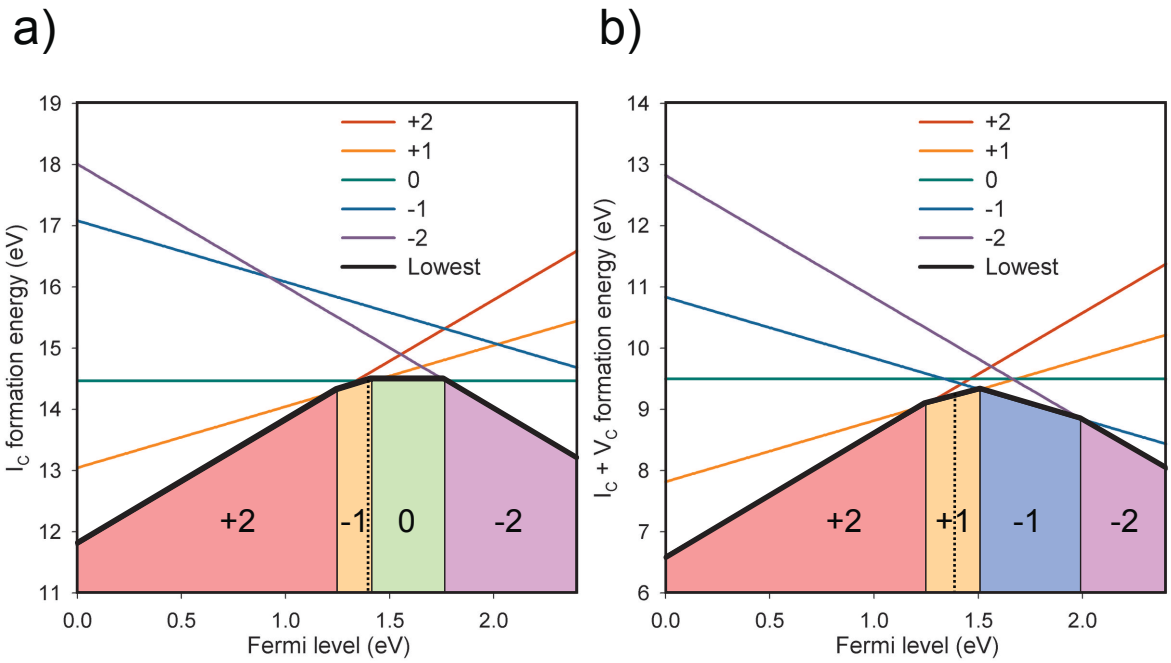

Figure 6: The formation energy for the accommodation of I at a) the carbon vacancy and b) carbon divacancy as a function of the Fermi level. Values are reported up to the experimental band gap limit of 2.39 eV. The calculated band gap limit of 1.38 eV is shown by the dotted line.

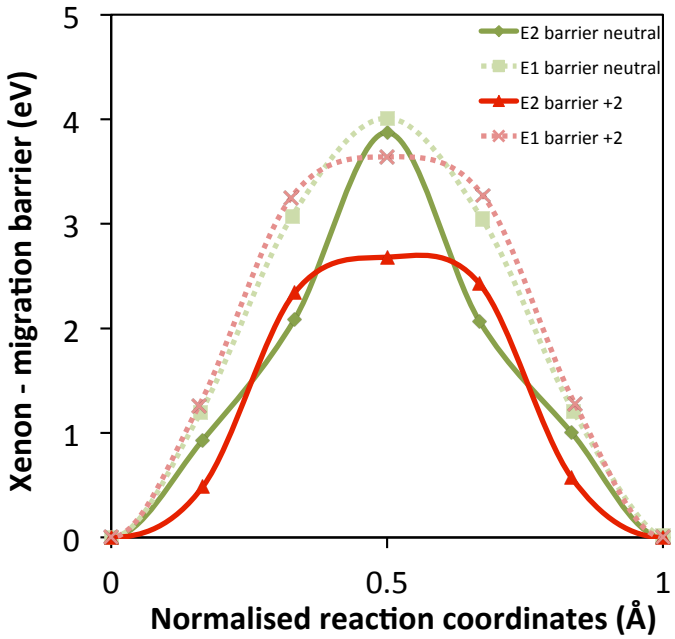

Figure 7: The migration barrier for the impurity-vacancy exchange rate (E_2) and rotation rate (E_1) for Xe in a charge neutral (green) and a +2 supercell (red).

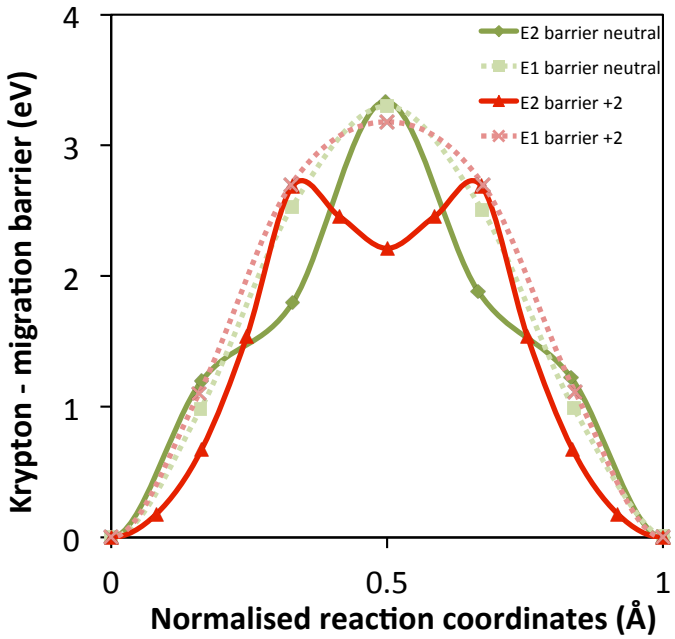

Figure 8: The migration barrier for the impurity-vacancy exchange rate (E_2) and rotation rate (E_1) for Kr in a charge neutral (green) and a +2 supercell (red). .

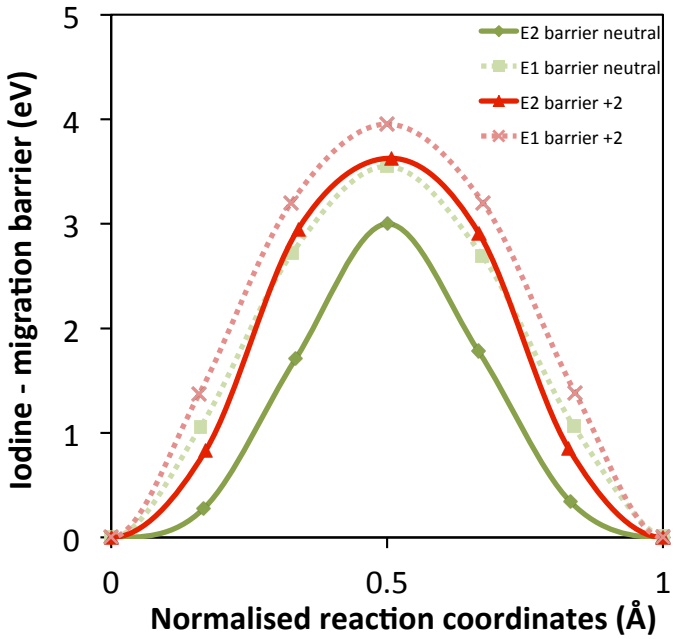

Figure 9: The migration barrier for the impurity-vacancy exchange rate (E_2) and rotation rate (E_1) for I in a charge neutral (green) and a +2 supercell (red).

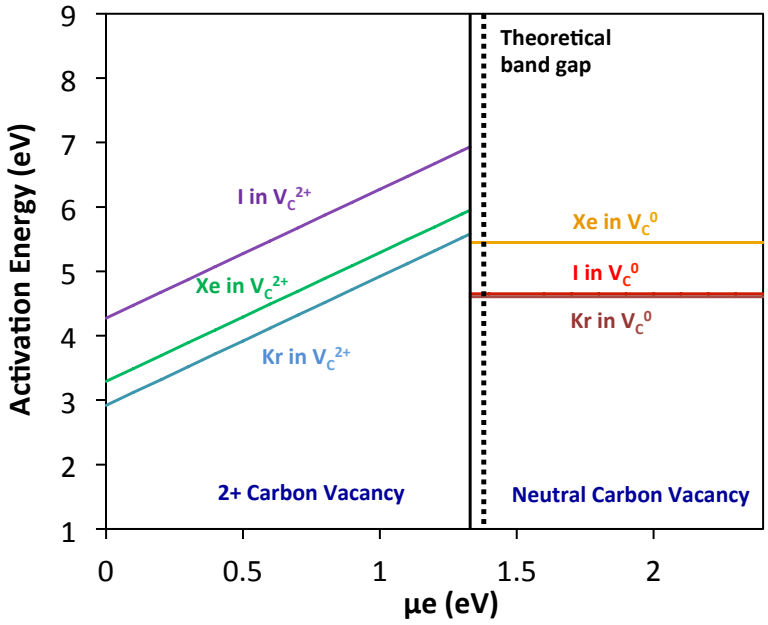

Figure 10: The activation energy for Xe, Kr and I as a function of the Fermi level. The Fermi level below which charge carbon vacancies are dominant is identified by a vertical black line. The range of values are dictated by the experimental band gap of 2.39 eV and the energy below which +2 carbon vacancies are more favourable is shown by the black line. The calculated band gap limit of 1.38 eV is shown by the dotted line.